Kinematic Rupture Model and Hypocenter Relocation of the 2013 M_w 6.6 Lushan Earthquake Constrained by Strong-Motion and Teleseismic Data

by Yong Zhang, Rongjiang Wang, Yun-tai Chen, Lisheng Xu, Fang Du, Mingpei Jin, Hongwei Tu, and Torsten Dahm

Online Material: Tables of 1D velocity structure, hypocentral locations, and kinematic rupture model.

INTRODUCTION

On 20 April 2013, an M_w 6.6 earthquake struck Lushan, Sichuan province, China (hereafter as Lushan earthquake), which caused 196 deaths and 21 missing. As another disastrous earthquake occurred on the Longmenshan fault after the 2008 M_w 7.9 Wenchuan earthquake, the Lushan earthquake stimulated an extensive discussion about its seismogenesis. In particular, whether it was a large aftershock of the 2008 M_w 7.9 Wenchuan earthquake has been heatedly debated (Chen *et al.*, 2013; Du *et al.*, 2013; Liu, Yi, *et al.*, 2013; Wang *et al.*, 2013; Jia *et al.*, 2014). Actually, after the Wenchuan earthquake, an increased seismic hazard for the southwest of the Longmenshan fault has been commonly recognized (Parsons *et al.*, 2008; Toda *et al.*, 2008). The occurrence of the Lushan earthquake seems to have confirmed this common understanding, and further attracts attention on the re-evaluation of future seismic activities on the southwest Longmenshan fault (Chen *et al.*, 2013). As the basis of these discussions, the source characteristics of the Lushan earthquake need to be well understood.

As a routine work for fast source earthquake information, Zhang *et al.* (2013) released the preliminary teleseismic rupture model about three hours after the Lushan earthquake. Their results show that the earthquake has no dominant rupture direction. The major slip area is located around the hypocenter and does not reach the surface.

It is known, however, that teleseismic data can only constrain the ruptured area relatively to the hypocenter (rupture initiation point). In contrast, near-field strong-motion data can provide information useful in precisely and accurately locating the fault rupture. Conversely, selection of the hypocenter location may significantly impact the results of the strong-motion data inversion. If the assumed hypocenter location is incorrect, the inversion will result in an unreliable rupture direction and distortion of Doppler effects, leading to a large misfit between synthetic and observed waveforms. This problem has been encountered already by Hartzell and Mendoza (1991) in their study of the 1978 Tabas, Iran, earthquake. Actually, the inaccurate hypocenter location is always a problem in the analysis of near-field data (both seismic and geodetic data; Hartzell and Mendoza, 1991; Jackson *et al.*, 2006; Zhang *et al.*, 2012), especially when the hypocenter uncertainty is not negligible compared with the source dimension (i.e., fault size). In the source inversion of the 2009 L'Aquila earthquake, Zhang *et al.* (2012) have shown that it is feasible to relocate the hypocenter by a joint inversion of the rupture process with teleseismic and near-field Interferometric Synthetic Aperture Radar data.

In this work, we relocate the hypocenter of the Lushan earthquake by inverting the near-field strong-motion data. Based on the relocated hypocenter, we then update the kinematic rupture model of the earthquake by jointly inverting the strong-motion and teleseismic data. The approach helps to constrain the nonuniqueness of sole teleseismic or sole near-field strong-motion kinematic inversions. Finally, we discuss the increased seismic hazard on the southwest Longmenshan fault after the Lushan earthquake.

HYPOCENTER RELOCATION WITH NEAR-FIELD STRONG-MOTION DATA

The southwest part of the Longmenshan fault zone consists of at least three major parallel faults, all of which are dominated by similar thrust mechanisms (Fig. 1a) (Deng *et al.*, 2003), resulting from the continental collision of the Tibetan plateau from northwest to southeast against the Sichuan basin. The focal mechanism of the Lushan earthquake is given by strike $=$ 218°, dip $=$ 39°, and rake $=$ 103° according to the *W*-phase moment tensor solution of the U.S. Geological Survey (USGS;
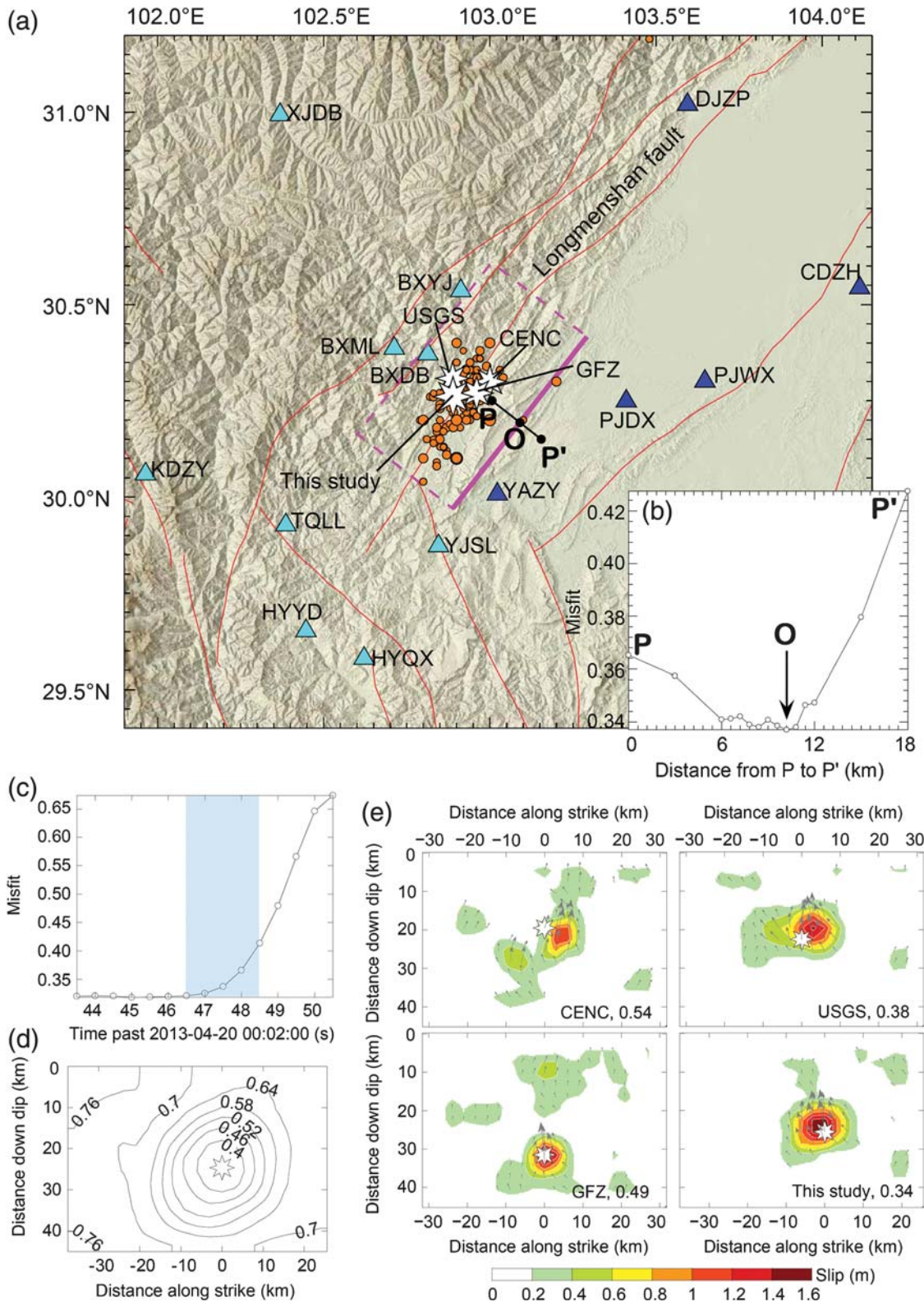
▲ **Figure 1.** (a) Strong-motion stations (cyan and blue triangles are those located in Tibetan plateau and Sichuan basin, respectively), surface projection of final determined fault position (pink rectangular), aftershocks (orange circles), and hypocenters (white stars) of the mainshock determined by CENC, USGS, GFZ, and this study. The red lines are the active faults (Deng *et al.,* 2003) in the epicentral area. (b) Misfit curve of the fault position. (c) Misfit curve of the origin time. (d) Misfit map of the hypocenter location by fixing the origin time and fault position as shown in (a). (e) Fault slip distributions obtained with the hypocenters of CENC, USGS, GFZ, and this study, respectively. The misfits based on these four hypocenters are marked by the lower right number in each subplot.

, last accessed October 2013). The hypocenter was located at 30.3° N, 103.0° E, depth 13 km by China Earthquake Networks Center (CENC), at 30.308° N, 102.888° E, depth 14 km by USGS, and at 30.27° N, 102.96° E, depth 19 km by German Research Center for Geosciences (GFZ), all indicating that the earthquake activated a southeast branch to the Sichuan basin side of the Longmenshan fault in the Lushan region.

In our fault-slip inversions, a sufficiently large potential fault plane of 63 km long and 45 km wide (Fig. 1a) is chosen and divided into 21 × 15 subfaults. Three-component accelerograms recorded by 14 strong-motion stations (Fig. 1a) are used for the inversions, except for the north–south component of station TQLL which shows large baseline shifts during the strong shaking period. Thus, totally we have data including 41 accelerograms for the inversions. These accelerograms are integrated to velocity seismograms and then filtered by a bandpass of 0.02–0.40 Hz. The lower-frequency cutoff is necessary to remove the effects caused by baseline shifts, which exist in all strong-motion records, whereas the upper frequency cutoff of 0.40 Hz is consistent with the subfault resolution of 3 km × 3 km.

Synthetic Green's functions are calculated using the code of Wang (1999). Because the earthquake occurred on the edge between Tibetan plateau and Sichuan basin, the velocity structure and topography is quite complicated within the spatial coverage of the strong-motion stations. Moreover, the strong-motion seismograms in the frequency range we used are dominated by the S waves for which waveform and arrival are more sensitive to the velocity structure than the P waves. To take into account for the complex velocity structure, we used two different crustal velocity structures (Ⓔ Table S1 available as an electronic supplement to this article) for the stations located in the Tibetan plateau (cyan triangles in Fig. 1a) and those in the Sichuan basin (blue triangles in Fig. 1a), respectively, when calculating Green's functions. In addition, the topography effect on the wave arrivals is minimized using a source-depth correction depending on the station elevation.

To invert the strong-motion data for the kinematic rupture process of the earthquake, we use the linear inversion approach of Zhang et al. (2012) based on the principle of least-squares optimization. During the linear inversion, several earthquake parameters need to be fixed, which are (1) the hypocenter location on the fault plane; (2) the origin time of the earthquake; and (3) the fault geometry parameters including the fault position, the strike, and dip angles. Results from the inversion for each subfault are time histories of the moment rate, also called the source time function (STF) and slip direction (rake angle). For numerical stability, the linear inversion approach needs generally to restrict the degree of freedom. This is realized using certain a priori constraints on the rupture process, which include in the present case that (1) the rupture starts at the hypocenter and propagates outward with a velocity not faster than 3 km/s (i.e., no super-shear rupture is considered); (2) the maximum rupture duration of each subfault is 6 s, in which there are 12 equidistant triangles (with varying but non-negative amplitudes) used to describe the slip time process; and (3) the rake angle is allowed only to vary within ±45° around the USGS estimate of 103°. Differently to most nonlinear inversion approaches, we do not need any constraints on the form of the STFs, but determine them automatically by the data.

For each given fault geometry (strike, dip, and location) and origin time, we perform a number of inversions by varying the hypocenter location on the fault plane. The optimal hypocenter location is then determined by the one leading to the best fit between synthetic and observed strong-motion waveforms. Actually, this is another approach for the hypocenter location; it uses the complete near-field waveform data instead of only the arrival times of seismic waves.

In principle, we next need to vary the fault geometry and origin time to find the best-fit hypocenter location. However, this would mean a grid search in a 6D parameter space (strike, dip, origin time, 1D fault position perpendicular to the strike, and 2D hypocenter position on the fault plane), which requires a huge computational effort, besides a number of trade-off problems among the six parameters. Considering that the teleseismic focal solution is almost independent of the hypocenter location, we only optimize the fault position and origin time, but discuss uncertainties in the strike and dip angles as well as their impacts later. Fixing the fault strike and dip, the location problem is reduced to a grid search in a 4D parameter space. Our results show that there is no strong trade-off between the origin time and the fault position. The misfit curves for these two parameters are nearly independent from each other and are shown in Figure 1b and c, respectively. Because of the relatively conservative a priori constraints on the rupture area, the rupture velocity, and the rupture duration, it appears that the earlier the origin time is selected, the better are the waveform fits. The phenomenon can be easily explained. In the extreme case, that is, without the a priori constraints, the model space with an earlier origin time has always a larger degree of freedom than that with a subsequent origin time, and thus can fit the data more easily. Based on the synthetic tests, which will be discussed later, we found that the optimal origin time should appear where the misfit begins to significantly increase. Because the cutoff frequency used is 0.40 Hz, the resolution of the origin time cannot be higher than 1–2 s. Actually, a range of about 1–2 s around 20 April 2013, 00:02:47.5 can be identified, after when the misfit starts to increase rapidly. Because this range of potential origin time is not sensitive to the fault position, and most origin times lead to similar hypocenter locations (Ⓔ Table S2 available as an electronic supplement to this article), we therefore fix the origin time at 47.5 s, which is equal to that released by the USGS. With this origin time, we get the fault position with the minimum waveform misfit as shown in Figure 1b. The corresponding best-fit hypocenter is located at 30.261° N, 102.889° E, depth 16.0 km (Fig. 1d).

Our relocated hypocenter is about 11.9, 5.6, and 7.5 km apart from those released by the institutions of CENC, USGS, and GFZ, and 8.6 and 9.0 km from those by Lv et al. (2013)

and Zhang and Lei (2013), respectively. The latter two groups relocated the hypocenter using the double-difference method. To demonstrate the influence of the hypocenter on the inversion results, we compare the slip distributions obtained based on three different hypocenters of CENC, USGS, and GFZ (Fig. 1e). They show non-negligible differences in rupture direction, slip area, maximum slip, and misfit. The fault slip distribution based on our relocated hypocenter (Fig. 1e) shows a circular rupture event without predominant rupture direction, which is consistent with the manual teleseismic inversion results by Liu, Zheng, et al. (2013) and Zhang et al. (2013) and the automatic teleseismic inversion results by S. Heimann (personal comm., 2013).

JOINT INVERSION WITH STRONG-MOTION AND TELESEISMIC DATA

The teleseismic data used in this study are provided by Incorporated Research Institutions for Seismology (IRIS). We selected 31 stations at epicentral distances between 30° and 90° with a roughly homogeneous coverage on the azimuth and take-off angles (Fig. 2). Only vertical components of the P waves are used, differently to the strong-motion data, from which all three components of the complete waveform are used. Green's functions for the teleseismic stations are generated based on the AK135 continental earth model (Kennett et al., 1995).

We totally have 41 and 31 waveform channels from the strong-motion and teleseismic datasets, respectively. In the joint inversion, each channel of the data is normalized by its signal energy (integral of squared velocity seismograms) so that
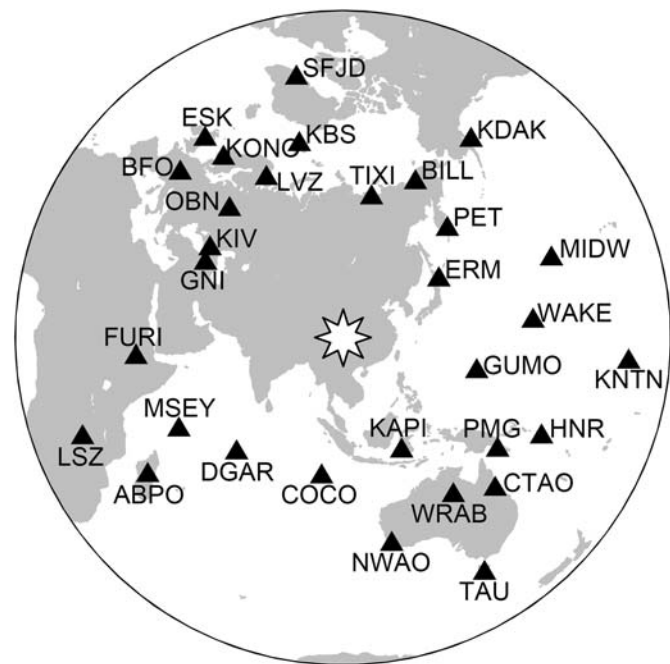
they are equally weighted in the sense of waveform. The results of the joint inversion are shown in Figure 3. The scalar seismic moment is estimated to be about 1.26×10^{18} N·m, equivalent to a moment magnitude of M_w 6.67. The source process is characterized by a single subevent (Fig. 3a), with most energy released within the first 10 s, consistent with the existing studies (Liu, Zheng, et al., 2013; Zhang et al., 2013). The fault slip is mainly concentrated around the hypocenter with a dimension of about 20 km (Fig. 3b and c). The maximum slip is about 1.2 m, slightly smaller than that inverted from the strong-motion data only. The strong-motion and teleseismic waveforms are both well fitted by the synthetics (Fig. 3d–e). Ⓔ The digital rupture model obtained by the joint inversion is available in the electronic supplement to this article.

Unlike the nonlinear inversion, the rupture front cannot be uniquely determined from the linear inversion results. Following the work of Lee et al. (2006), we assume that the rupture front reaches the subfault when the accumulated slip exceeds 0.05 m. The slip-weighted average rupture velocity found in this way is about 2.3 km/s, or 0.6–0.7 of the S-wave velocity in the upper crust.

The joint inversion shows a smoother slip distribution and smaller maximum slip than those derived from the strong-motion data only. It could be attributed to the relative poor spatial resolution ability of the teleseismic data. In addition, it suggests that the second subevent obtained by inverting only the teleseismic data (Zhang et al., 2013) is not evident.

DISCUSSION AND CONCLUSIONS

Recently many near-field strong-motion data are available shortly after an earthquake. Such data, combined with teleseismic records and a proper relocation of the hypocenter, have the potential to significantly improve kinematic rupture and slip models, which may otherwise be inherently nonunique. In the case of the Lushan earthquake, we have demonstrated significant influences of hypocenter uncertainties on the inversion results using near-field strong-motion data. The problem is less serious for large earthquakes if the fault extension is much larger than the hypocenter uncertainty. However, once the fault size is comparable to, or even smaller than, the hypocenter uncertainty, different hypocenters certainly result in different apparent rupture processes.

In this paper, we use the linear inversion method to optimize the hypocenter of the Lushan earthquake by trying different fault positions and origin times with fixed strike and dip angles. In principle, this work can also be done by a nonlinear network inversion method, which, however, would cost much more in computational efforts. In fact, if using the nonlinear inversion approach, at least two more parameters for each subfault, that is, the rupture time and the rupture duration, need to be optimized in a nonlinear way. In addition, it should be noticed that the nonlinear inversion approach uses generally a preselected shape for the subfault STF, which may lead to certain artifact. To check the reliability of the result, a

▲ **Figure 2.** Epicenter (white star) and teleseismic stations (black triangles).
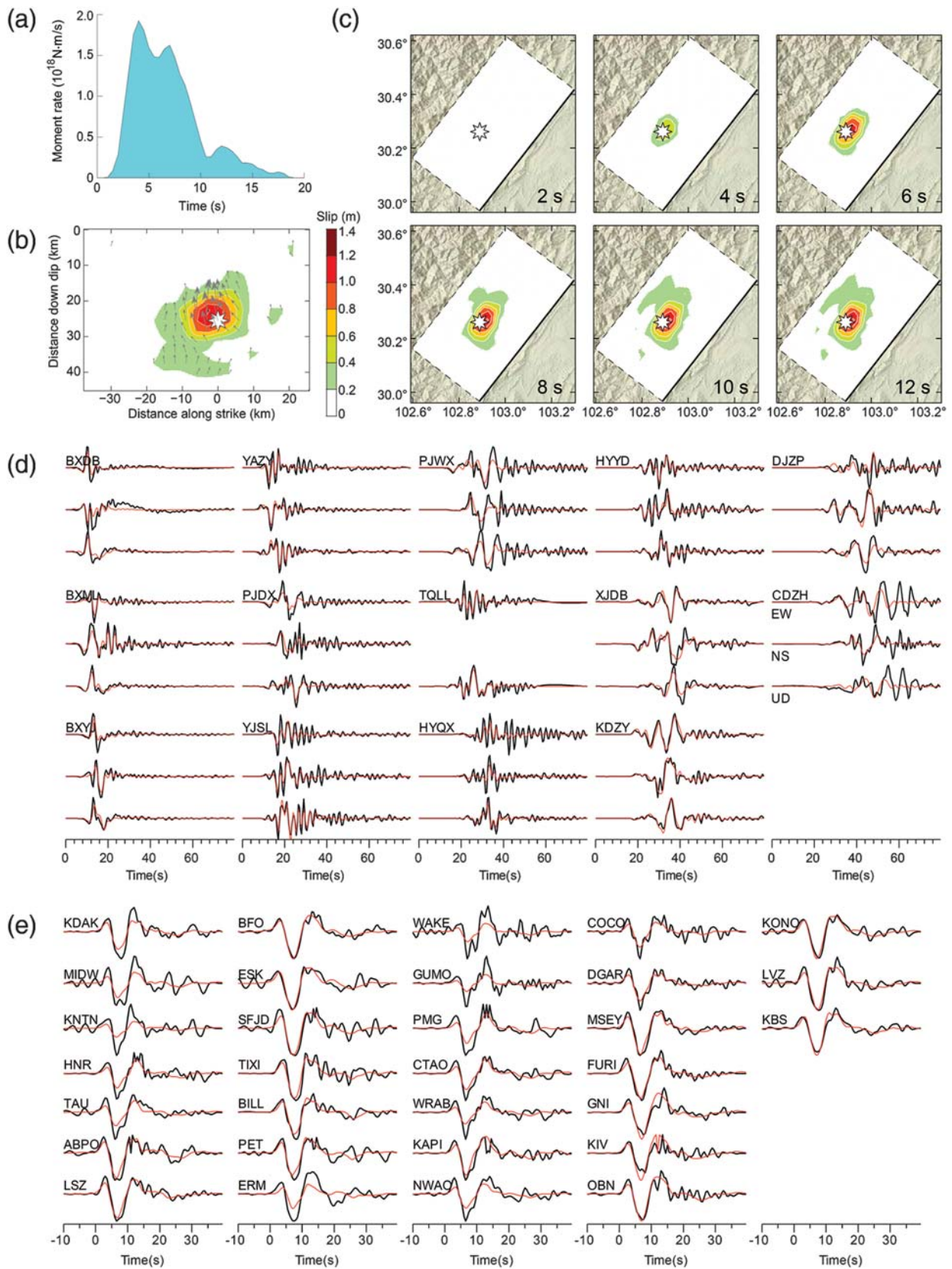
▲ **Figure 3.** Results from joint inversion of the strong-motion and teleseismic data. (a) Source time function, (b) static fault slip distribution, (c) temporal variations of the surface projection of fault slip distributions, (d) comparisons between observed (black) and synthetic (red) strong-motion waveforms, (e) comparisons between observed (black) and synthetic (red) teleseismic waveforms. The time zeros in (d) and (e) are the earthquake origin time and *P* arrivals, respectively.
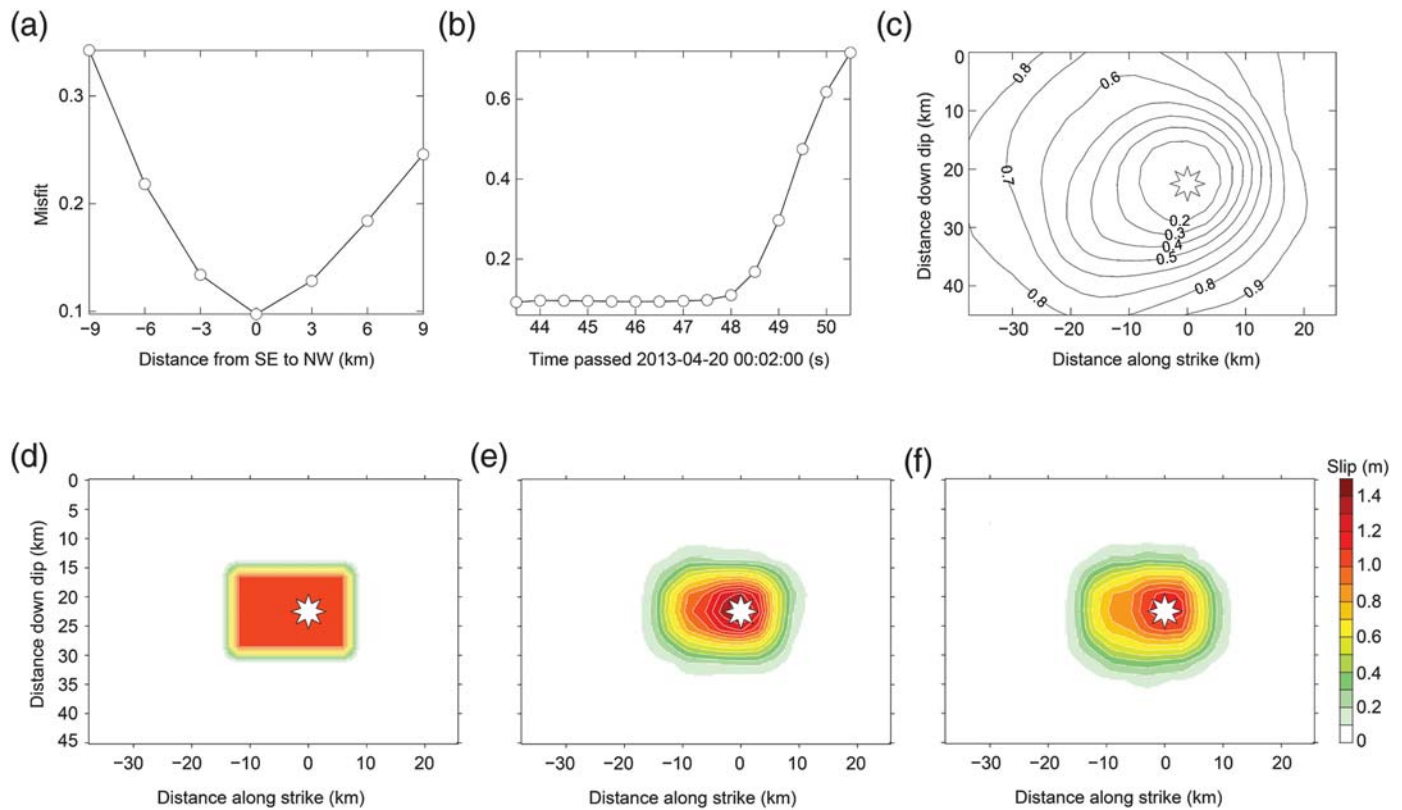
▲ **Figure 4.** Resolution test for the Lushan earthquake. (a) Grid search for the fault position through the strong-motion inversion. The assumed fault position corresponds to 0. (b) Grid search for the origin time with strong-motion data. The assumed origin time is 47.5 s. (c) Misfit of all subfaults as hypocenters in the strong-motion inversion based on the optimized origin time and fault position. (d) The input fault slip model. (e) Slip distribution from the strong-motion inversion. (f) Slip distribution from the joint inversion of the strong-motion and teleseismic data.

resolution test is performed. A rectangular slip area is assumed on the fault, and then synthetic strong-motion and teleseismic waveform data are generated and added with 10% Gaussian noise. It is shown in Figure 4 that the fault position and hypocenter are both well determined, but the origin time is relatively less resolved (Fig. 4a–c). The hypocenter determined is stable when varying the origin time by ±1 s, suggesting that uncertainties in the origin time may not be critical for our rupture location.

In the resolution test, the fault slip can be generally well retrieved by either jointly inverting the synthetic strong-motion and teleseismic data or inverting only the strong-motion data (Fig. 4d–f). It is noticed that the slip distribution of the joint inversion is smoother than that from the strong-motion data inversion. As mentioned above, it may be attributed to the relative poor spatial resolution ability of the teleseismic data. Though the synthetic test does not show any obvious advantage of the joint inversion, it is always useful in practice because results by only using the near-field strong-motion data are more sensitive to the fault location and fault irregularities. The latter are usually not well known. Therefore, although the strong-motion data can resolve more details of source ruptures, it usually leads to large uncertainties caused by the local 3D structure effect. In contrast, teleseismic data result in a smoother slip model, but it is less sensitive to the hypocenter location and local crust structure, and thus can help to estimate the major rupture pattern (relative to the hypocenter) more reliably. The complementary advantages of the two datasets can be combined by the joint inversion. In addition, the joint use of the near-field strong-motion and teleseismic data can increase the coverage of take-off angle on the ruptured fault and therefore improve the resolution of the slip distribution particularly with depth.

In the above analysis, we do not consider the impacts of the fault strike and dip angles. Nowadays, uncertainties in teleseismic focal solutions (i.e., strike and dip) are about 10° (Helffrich, 1997). To check their influences on the hypocenter location through the strong-motion inversion, we change the strike and dip of the Lushan earthquake by ±10° and compare the corresponding location results. Ⓔ As shown in Table S3 available as an electronic supplement to this article, these changes do not significantly disturb the hypocenter location. The maximum difference among the five hypocenters including the preferred one is about 6 km in the horizontal distance and 4 km in depth, which could be considered as the upper limit of uncertainties in our hypocenter location.

The joint inversion based on the relocated hypocenter shows a simple rupture process of the Lushan earthquake with

a comparable spatial extension along the strike and dip directions, which is typical of most moderate earthquakes. The ruptures occurred in the upper crust, but did not breach the surface. This could explain why the earthquake damages mainly concentrated on the hanging wall, instead of the areas around the extrapolated surface trace of the fault (Zhang et al., 2013).

To investigate how the local bilateral velocity structure influences the hypocenter location, we also carried out the inversions using an average crust model (Ⓔ Table S1 available as an electronic supplement to this article) based on CRUST2.0 (Bassin et al., 2000). No substantial changes on the rupture pattern are found, but the source becomes systematically shallower by about 2 km and the root mean square misfit to the strong-motion data increases by 20%. Additionally, when using the average velocity model, the hypocenter coincides with the slip centroid and no dominant rupture directivity is visible. In comparison, the bilateral velocity model shifts the hypocenter 2–3 km apart from the slip centroid, so that slight up-dip rupture directivity appears (Fig. 3b). However, we notice that this directivity effect is not significant because the uncertainty of our hypocenter location is twice larger than 2–3 km.

It is widely accepted that the Lushan earthquake is closely related to the 2008 Wenchuan earthquake (Chen et al., 2013; Du et al., 2013; Liu, Yi, et al., 2013; Wang et al., 2013). In this work, it is found that the major slip area of the Lushan earthquake is about 40–50 km apart from the southwest end of the 2008 Wenchuan earthquake fault, suggesting that there is a wide area unruptured southwest of Longmenshan fault. Because the Lushan earthquake only ruptured a small fault segment, increased seismic hazards in its adjacent regions, particularly in the gap to the Wenchuan earthquake, should be noticeable. ⬙

ACKNOWLEDGMENTS

REFERENCES

Bassin, C., G. Laske, and G. Masters (2000). The current limits of resolution for surface wave tomography in North America, *Eos Trans. AGU* **81,** F897.

Chen, Y., Z. Yang, Y. Zhang, and C. Liu (2013). From 2008 Wenchuan earthquake to 2013 Lushan earthquake (in Chinese), *Sci. China Ser. D.* **43,** 1064–1072.

Deng, Q., P. Zhang, Y. Ran, X. Yang, W. Min, and Q. Chu (2003). Basic characteristics of active tectonics of China, *Sci. China Ser. D.* **46,** no. 4, 356–372.

Du, F., F. Long, X. Yuan, G. Yi, Y. Gong, M. Zhao, Z. Zhang, H. Qiao, Z. Wang, and J. Wu (2013). The M 7.0 Lushan earthquake and the relationship with the M 8.0 Wenchuan earthquake in Sichuan, China (in Chinese), *Chin. J. Geophys.* **56,** no. 5, 1772–1783.

Hartzell, S. H., and C. Mendoza (1991). Application of an iterative least-squares wave-form inversion of strong-motion and teleseismic records to the 1978 Tabas, Iran, earthquake, *Bull. Seismol. Soc. Am.* **81,** no. 2, 305–331.

Helffrich, G. R. (1997). How good are routinely determined focal mechanisms? Empirical statistics based on a comparison of Harvard, USGS and ERI moment tensors, *Geophys. J. Int.* **131,** 741–750.

Jackson, J., M. Bouchon, E. Fielding, G. Funning, M. Ghorashi, D. Hatzfeld, H. Nazari, B. Parsons, K. Priestley, M. Talebian, M. Tatar, R. Walker, and T. Wright (2006). Seismotectonic, rupture process, and earthquake-hazard aspects of the 2003 December 26 Bam, Iran, earthquake, *Geophys. J. Int.* **166,** 1270–1292.

Jia, K., S. Zhou, J. Zhuang, and C. Jiang (2014). Analysis on the possibility of the independence between the 2013 Lushan earthquake and the 2008 Wenchuan earthquake on Longmen Shan fault, Sichuan, China, *Seismol. Res. Lett.* **85,** no. 1, 60–67, doi: 10.1785/0220130115.

Kennett, B. L. N., E. R. Engdahl, and R. Buland (1995). Constraints on seismic velocities in the earth from traveltimes, *Geophys. J. Int.* **122,** 108–124.

Lee, S., K. Ma, and H. Chen (2006). Three-dimensional dense strong motion waveform inversion for the rupture process of the 1999 Chi-Chi, Taiwan, earthquake, *J. Geophys. Res.* **111,** no. B11308, doi: 10.1029/2005JB004097.

Liu, C., Y. Zheng, C. Ge, X. Xiong, and H. Xu (2013). Rupture process of the M 7.0 Lushan earthquake, *Sci. China Earth Sci.* **43,** no. 6, 1020–1026, doi: 10.1007/s11430-013-4639-9.

Liu, J., G. Yi, Z. Zhang, Z. Guan, X. Ruan, F. Long, and F. Du (2013). Introduction to the Lushan, Sichuan M 7.0 earthquake on 20 April 2013 (in Chinese), *Chin. J. Geophys.* **56,** no. 4, 1404–1407.

Lv, J., X. Wang, J. Su, L. Pan, Z. Li, L. Yin, X. Zeng, and H. Deng (2013). Hypocentral location and source mechanism of the M_s 7.0 Lushan earthquake sequence (in Chinese), *Chin. J. Geophys.* **56,** no. 5, 1753–1763.

Parsons, T., J. Chen, and E. Kirby (2008). Stress changes from the 2008 Wenchuan earthquake and increase hazard in the Sichuan basin, *Nature* **454,** 509–510.

Toda, S., J. Lin, M. Meghraoui, and R. S. Stein (2008). 12 May 2008 $M = 7.9$ Wenchuan, China, earthquake calculated to increase failure stress and seismicity rate on three major fault systems, *Geophys. Res. Lett.* **35,** L17305, doi: 10.1029/2008GL034903.

Wang, R. (1999). A simple orthonormalization method for stable and efficient computation of Green's functions, *Bull. Seismol. Soc. Am.* **89,** no. 3, 733–7410.

Wang, W., J. Hao, and Z. Yao (2013). Preliminary result for rupture process of Apr. 20, 2013, Lushan earthquake, Sichuan, China (in Chinese), *Chin. J. Geophys.* **56,** no. 4, 1412–1417.

Zhang, G., and J. Lei (2013). Relocation of the Lushan, Sichuan strong earthquake (M_s 7.0) and its aftershocks (in Chinese), *Chin. J. Geophys.* **56,** no. 5, 1764–1771.

Zhang, Y., Y. Chen, and L. Xu (2013). Rupture process of the Lushan 4.20 earthquake and preliminary analysis on the disaster-causing mechanism (in Chinese), *Chin. J. Geophys.* **56,** no. 4, 1408–1411, doi: 10.6038/cjg20130435.

Zhang, Y., W. Feng, Y. Chen, L. Xu, Z. Li, and D. Forrest (2012). The 2009 L'Aquila M_w 6.3 earthquake: A new technique to locate the hypocenter in the joint inversion of earthquake rupture process, *Geophys. J. Int.* **191,** 1417–1426, doi: 10.1111/j.1365-246X.2012.05694.x.

Yong Zhang[1]
Rongjiang Wang
Hongwei Tu[2]
Torsten Dahm
GFZ German Research Centre for Geosciences
Telegrafenberg
Potsdam 14473, Germany
wang@gfz-potsdam.de

Yun-tai Chen
Lisheng Xu
Institute of Geophysics
China Earthquake Administration
Beijing 100081, China

Fang Du
Earthquake Administration of Sichuan Province
Chengdu 610041, China

Mingpei Jin
Earthquake Administration of Yunnan Province
Kunming 650041, China

[1] Also at Institute of Geophysics, China Earthquake Administration, Beijing 100081, China.
[2] Also at Earthquake Administration of Qinghai Province, Xining 810001, China.